NANO · MICRO small
www.small-journal.com

Adjustable Ultra-Light Mechanical Negative Poisson's Ratio Metamaterials with Multi-Level Dynamic Crushing Effects

Xiang Xu, Chuanqiang Huang, Chongchong Li, Xin Wang, Xiaojie Li, Zhen Li,* Xiangchao Feng, Bingyang Li, Yong Zhang, Haibo Ji, and Pengfei Wang**

Mechanical metamaterials with multi-level dynamic crushing effects (MM-MLs) are designed in this study through coordinate transformation and mirror arrays. The mechanical effects of the diameter and length ratio of the struts and connecting rods, the Euler angles, and the cell numbers on the mechanical properties are investigated separately. MM-ML can exhibit significant two-level platform stress, and the local cells in the first platform stress stage undergo rotational motion, while the second platform stress stage mainly involves collapse compression and bending. Although increasing the length of the connecting rods can increase the range of Poisson's ratio, it will reduce the level of platform stress and energy absorption. Increasing the Euler angle will reduce the strain interval of the first platform stress and can improve the energy absorption capacity. In addition, increasing the cell number while maintaining a constant relative density can effectively enhance energy absorption. MM-ML has significant parameter controllability, can achieve different platform stress regions, different ranges of Poisson's ratios, and energy absorption requirements according to the application scenario, and can demonstrate functional diversity compared to existing research. The design scheme can provide ideas for adaptive crushing protection requirements.

1. Introduction

Lattice metamaterials have many excellent mechanical advantages, such as light weight,[1–3] high energy absorption,[4–6] and high strength,[7–9] and have enormous application potential in fields such as automobiles,[10] aerospace,[11] and medical equipment.[12] The mechanical properties of lattice metamaterials can be customized and adjusted by changing their microcell characteristics and macroscale parameters to meet different application scenarios and performance requirements.[13–16] Among them, lattice metamaterials with negative Poisson's ratio functions have attracted much attention due to their special deformation modes and excellent mechanical behavior.[17–19] Related researchers have conducted in-depth research on different negative Poisson's ratio lattice metamaterials using experimental, theoretical analysis, and numerical simulation methods, exploring the inherent relationship between the novel microstructure and mechanical properties of lattice metamaterials and laying the foundation for obtaining the optimal topology lattice design.

Usually, the Poisson's ratio of most materials is positive, which means that when the material is under pressure, its lateral size will decrease; when the material is stretched, its lateral size will increase. However, negative Poisson's ratio mechanical metamaterials exhibit opposite mechanical behaviors. When these materials are subjected to pressure or tension, their lateral dimensions increase rather than decrease. This unique mechanical property endows 2D negative Poisson's ratio mechanical metamaterials with potential application value in multiple fields. Due to their ability to absorb more energy under pressure or tension, negative Poisson's ratio mechanical metamaterials can be used as high-performance energy-absorbing materials. This material can be used to design safer structures for automobiles, aerospace, etc., to improve their energy absorption capacity in collision accidents.[20–22]

In addition, negative Poisson's ratio mechanical metamaterials can also be used to improve the mechanical properties and stability of materials. Due to their negative Poisson's ratio, these materials are able to better maintain their shape and structural stability under external forces, thereby improving their overall performance. Mizzi et al.[23] proposed a way to replace rotating material

X. Xu, C. Huang, C. Li, X. Li
School of Engineering
Anhui Agricultural University
Hefei 230036, China

X. Wang, Z. Li, X. Feng, B. Li, P. Wang
Advanced Materials and Energy Center
China Academy of Aerospace Science and Innovation
Beijing 100088, China
E-mail: wxtj_9449@stu.xjtu.edu.cn; yy2017@tsinghua.edu.cn; pengfeiwang@xjtu.edu.cn

B. Li
College of Engineering
Peking University
Beijing 100871, China

Y. Zhang
College of Mechanical Engineering and Automation
Huaqiao University
Xiamen 361021, China

H. Ji
National Key Laboratory of Mechanics and Control for Aerospace Structures
Nanjing University of Aeronautics and Astronautics
Nanjing 210016, China

The ORCID identification number(s) for the author(s) of this article can be found under https://doi.org/10.1002/smll.202403082

DOI: 10.1002/smll.202403082

blocks with hierarchical triangular truss networks to obtain a variety of lightweight auxetic metamaterials whose weight can be reduced by 80% to ensure that the original negative Poisson's ratio effect remains unchanged. To improve the mechanical properties of tetrachiral honeycombs (TCHs), Qin et al.[24] proposed two types of axisymmetric tetrachiral honeycombs (ATCHs). Under low-speed impact, ATCHs had greater specific energy absorption and more significant negative Poisson's ratio effects than did TCH, but axisymmetric honeycombs did not have an advantage at medium to high impact rates. Zhang et al.[25] proposed a novel concave antispin structure with arcuate ligaments and found that unique deformation patterns can be induced by rotation of the cylinder, contact interactions between the cylinder and ligaments, and petal-like cell interactions, and the normalized Young's modulus can be increased by 8 times and 4 times compared to that of energy absorption. Although mechanical metamaterials with negative Poisson's ratios have excellent mechanical properties, their low stiffness limits their development. Based on existing research, Wang et al.[26] developed an asymmetric mechanical metamaterial with star-shaped characteristics, the star-shaped circular honeycomb (SCH), which can be reasonably customized for engineering applications with different mechanical property requirements. Nikolić et al.[27] proposed an improved negative Poisson's ratio 2D arc star structure, which obtained a higher negative Poisson's ratio and improved material utilization compared with the initial scheme. To further improve the mirror symmetry of traditional concave negative Poisson's ratio crystal cells, Mahnama et al.[28] proposed an innovative auxetic metamaterial with asymmetric crystal cells. Compared with the baseline symmetric unit honeycomb, the proposed metamaterial exhibits significant specific energy absorption characteristics and excellent expansion properties. The above studies revealed that multiple types of innovative 2D negative Poisson's ratio mechanical metamaterials have made significant breakthroughs in performance improvement. Wide-range Poisson's ratio and impact resistance have gradually been explored, but negative Poisson's ratio mechanical metamaterials with 2D cross-sectional characteristics have limited their application scenarios and further breakthroughs in mechanical properties due to their single geometric properties.

To expand the application scenarios of mechanical metamaterial design, the design and analysis methods of 3D lattice cells with negative Poisson's ratios are gradually being promoted.[29] For example, Zhao et al.[30] utilized Abaqus for secondary development and developed plug-in tools for simulation analysis of star-shaped honeycombs (SHs), double-headed arrow honeycombs (DAHs), and re-entry hexagonal honeycombs (RHHs). They validated the equivalent Poisson's ratio, elastic modulus, and platform stress based on homogenization theory. Cui et al.[31] proposed a novel crystal cell design scheme for specifying 3D lattice metamaterials with a negative Poisson's ratio, which can accurately predict a negative Poisson's ratio by establishing a theoretical formula containing complex mechanical quantities that control the deformation of metamaterial substructures. Luo et al.[32] developed a new lattice mechanical metamaterial with both ideal elastic isotropy and an extremely negative Poisson's ratio via a topology optimization method. With this method, a negative Poisson's ratio can be achieved at different relative densities by custom single-cell microlattices. Ma et al.[33] proposed a 3D hybrid double-arrowhead lattice structure with convex and concave quadrilateral components. In this lattice structure, the stress of the crushing platform increases when Poisson's ratio approaches zero, and the effect of Poisson's ratio weakens under high-speed crushing conditions. He et al.[34] proposed a new 3D negative Poisson's ratio energy absorption structure based on 2D nonconvex hexagonal elements. The fuselage cross-section with a 3D negative Poisson's ratio structure has a better energy absorption capacity than that without a 3D negative Poisson's ratio structure. Through in-depth exploration of the above research, it was found that most of the designs of negative Poisson's ratio mechanical metamaterials exhibit a single load effect. As energy absorption devices, they can only show a single mode of energy absorption under collision conditions, the impact force is often too concentrated, and the buffering and protection ability is limited.

If a design strategy with multi-level energy absorption is introduced, it may be possible to slow the impact force through the gradual deformation of multiple stages to reduce damage to protected objects or people. Therefore, on the basis of the excellent negative Poisson's ratio characteristic design, a mechanical metamaterial with a two-level loading effect is designed, and its mechanical behavior under dynamic impact conditions is studied in this study. This study is expected to provide ideas for multi-level energy absorption design in broader application scenarios.

2. Design Principles

To achieve excellent impact protection performance, the structure needs to meet many complex nonlinear mechanical requirements, such as a low initial peak collision force, long-stress platform, and high impact energy absorption. Due to their relatively simple geometric design, existing lightweight impact-resistant structures have difficulty simultaneously meeting many nonlinear impact performance requirements that are mutually constrained, thus absorbing a large amount of impact energy while maintaining a low impact force. Although many metamaterials used for collision protection can exhibit high energy absorption, they ignore the regulation of dynamic mechanical behavior in the process of energy absorption and can only experience a single platform stress,[35–38] as shown in **Figure 1a**. To improve the shortcomings of existing impact protection materials, decomposing a single load behavior is an effective improvement path for developing the multi-level load effect function of mechanical metamaterials. This type of mechanical metamaterial can provide many advantages, such as a low initial collision peak force, a long-stress platform, and high impact energy absorption.

Enabled by additive manufacturing techniques, researchers have subsequently investigated the energy absorption performance of octet-truss metamaterials made at the macro- or microscales. In this study, a mechanical metamaterial with multi-level loading effects (MM-ML) is constructed by transforming the octahedral structures of octet-truss metamaterials. A schematic diagram of the changes in the basic cellular characteristics of MM-ML is shown in Figure 1b,c. The periodic cells of MM-ML are mainly formed through three coordinate transformations and three mirror arrays of octahedral structures. To improve the

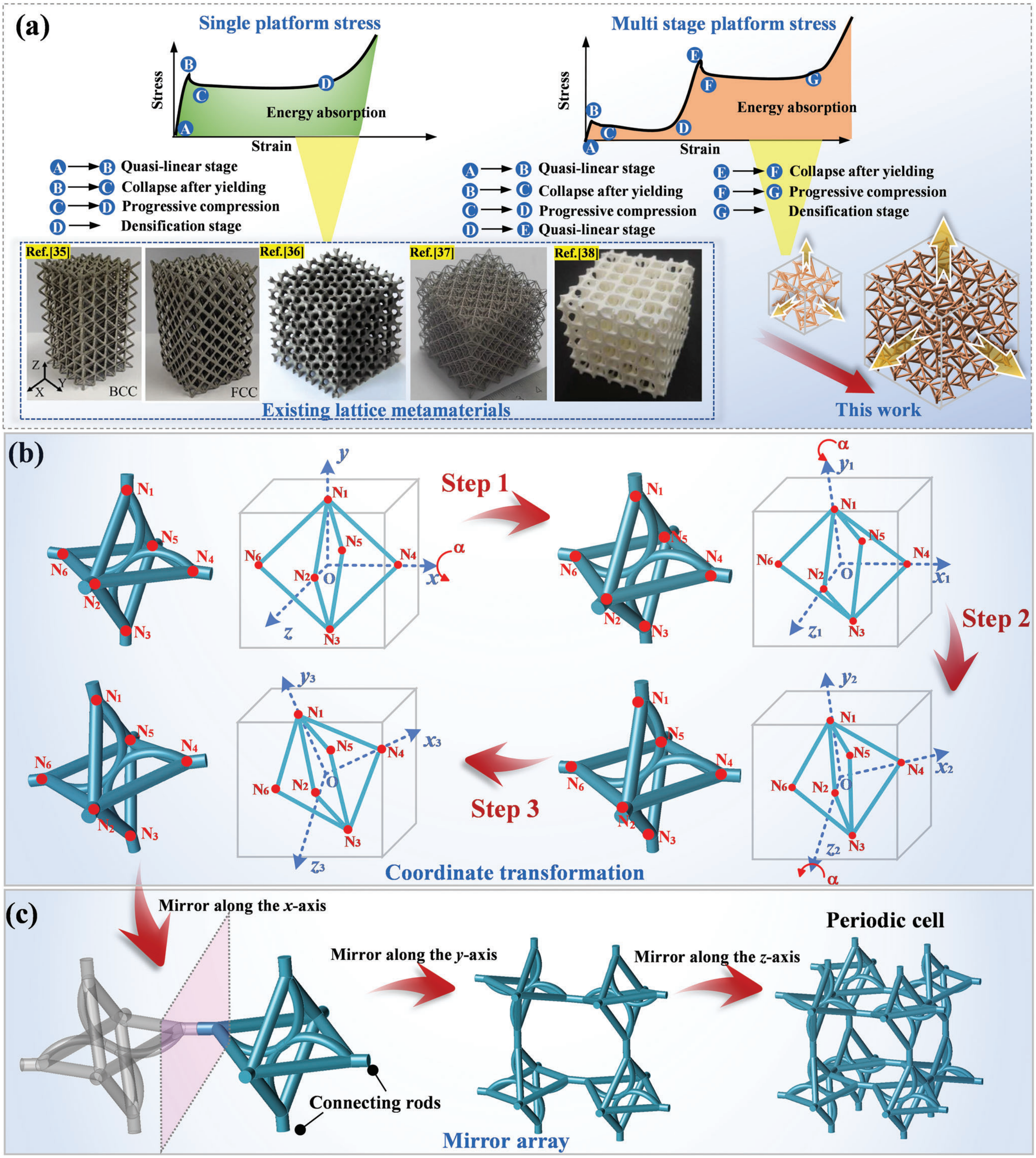

Figure 1. Schematic diagram of the periodic cell transformation in mechanical metamaterials. a) Load curves of different mechanical metamaterials. b) Coordinate transformation. c) Mirror transformation.

mechanical performance of traditional octahedral structures, double semicircular bars are designed in the planes where nodes N_1, N_4, N_3, and N_6 are located, and all the structures have the same diameter. After continuously rotating at a certain angle α around the x, y, and z coordinate axes, the octahedral structures obtain new positions and attitudes. Node O (0, 0, 0, 1) is defined as the center of the octahedral body, while node N_i (x_{N_i}, y_{N_i}, z_{N_i}, 1) (i = 1, 2..., 6) is the center of the eight faces. The rotation angle α is used to describe the Euler angle of the octahedral space attitude. The unit cell coordinate system O-xyz is established with

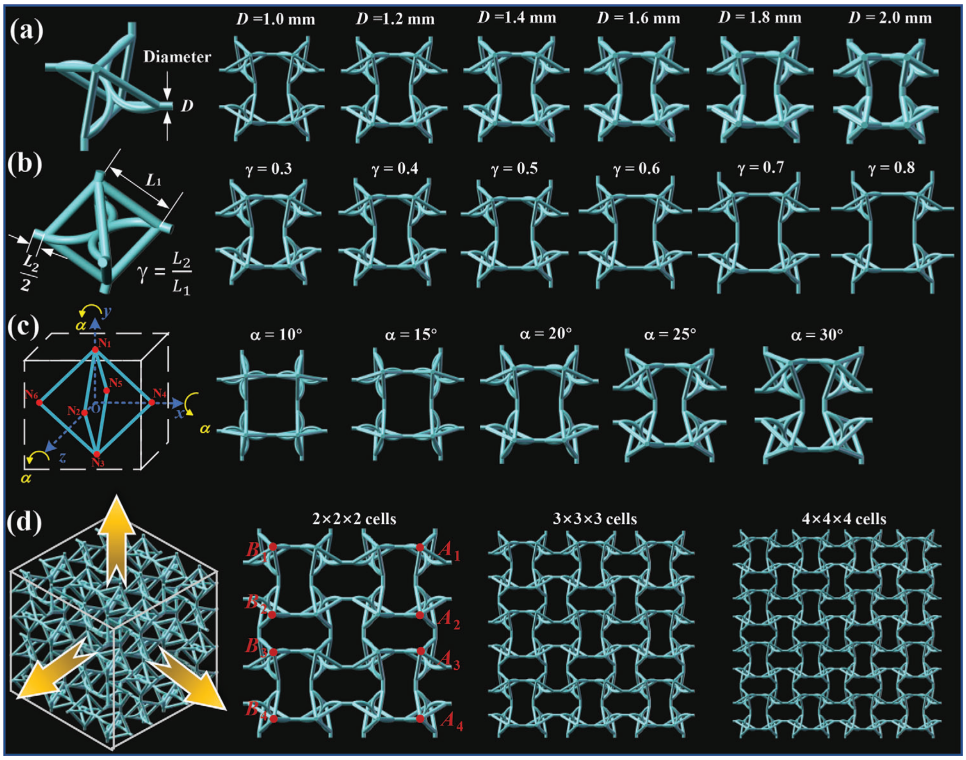

Figure 2. MM-ML with different design parameters. a) Different rod diameters. b) Different rod size proportions. c) Different Euler angles. d) Different cell arrangements.

the body center O of the octahedron as the origin. Taking the length of each supporting rod of the octahedral structures as L_1, the original nodal coordinate matrix of the octahedral structures $\mathbf{M}_o$ can be expressed as:

$$\mathbf{M}_o = \left[N_1\ N_2\ N_3\ N_4\ N_5\ N_6\right] = \frac{\sqrt{2}L_1}{2}\begin{bmatrix} 0 & 0 & 0 & 1 & 0 & -1 \\ 1 & 0 & -1 & 0 & 0 & 0 \\ 0 & 1 & 0 & 0 & -1 & 0 \\ 1 & 1 & 1 & 1 & 1 & 1 \end{bmatrix} \tag{1}$$

The improved octahedral structure achieves a change in its posture when rotating around the x, y, and z coordinate axes. The transformation matrix $\mathbf{T}_M$ of node N_i can be expressed as:

$$T_M = \begin{bmatrix} \cos^2(\alpha) & -\cos(\alpha)\sin(\alpha) & \sin(\alpha) & 0 \\ \cos(\alpha)\sin(\alpha) + \sin^2(\alpha)\cos(\alpha) & \cos^2(\alpha) - \sin^3(\alpha) & -\cos(\alpha)\sin(\alpha) & 0 \\ \sin^2(\alpha) - \cos^2(\alpha)\sin(\alpha) & \cos(\alpha)\sin(\alpha) + \sin^2(\alpha)\cos(\alpha) & \cos^2(\alpha) & 0 \\ 0 & 0 & 0 & 1 \end{bmatrix} \tag{2}$$

The coordinate matrix $\mathbf{M}_P$ of the center point N_i $(x_{N_i}, y_{N_i}, z_{N_i}, 1)$ (i = 1, 2..., 6) after coordinate transformation can be calculated using Equation (3).

$$\mathrm{M}_P = \mathrm{T}_M\ \mathrm{M}_o \tag{3}$$

After three coordinate rotations, the octahedral structure is mirrored with the end face of the connecting rod, as shown in Figure 1c. It should be noted that the normal vector of the connecting rod end face is parallel to the coordinate axis in the original coordinate O-xyz. Finally, the periodic basic cells of MM-ML are generated after three mirror transformations. On the basis of periodic cells, arrays of different scales can be designed according to the design requirements of metamaterials of different macroscopic sizes. The Euler angle α can be used as a controllable parameter to change the posture of periodic cells and can be used to adjust the mechanical performance range of metamaterials.

The topological configuration of periodic cells is related to their geometric dimensions and pose positions, so the design of periodic cells can be based on relevant characteristic parameters. As shown in **Figure 2**, by changing the different rod diameters, rod size ratios, Euler angles, and cell numbers of MM-ML, a series of more topological configurations of MM-ML can be derived.

L-PBF (Laser Powder Bed Fusion) technology is used as a manufacturing method for MM-MLs due to its advantages in processing high geometric resolution metal materials.[39–41] 316 L stainless steel is used as the matrix material, and due to its high sensitivity to the strain rate, it is necessary to explore its strain rate effect. The quasi-static tensile test of the matrix material was repeated three times on a universal material testing machine with a tensile speed of 1 mm/min. The dynamic compression of the material was conducted in a split Hopkinson pressure bar (SHPB) with a strain rate test range of 1500–5000 s^{-1}. In this SHPB, the signals coming from the gauges are evaluated in terms of the engineering stress σ, strain rate $\dot{\varepsilon}$, and strain ε, and

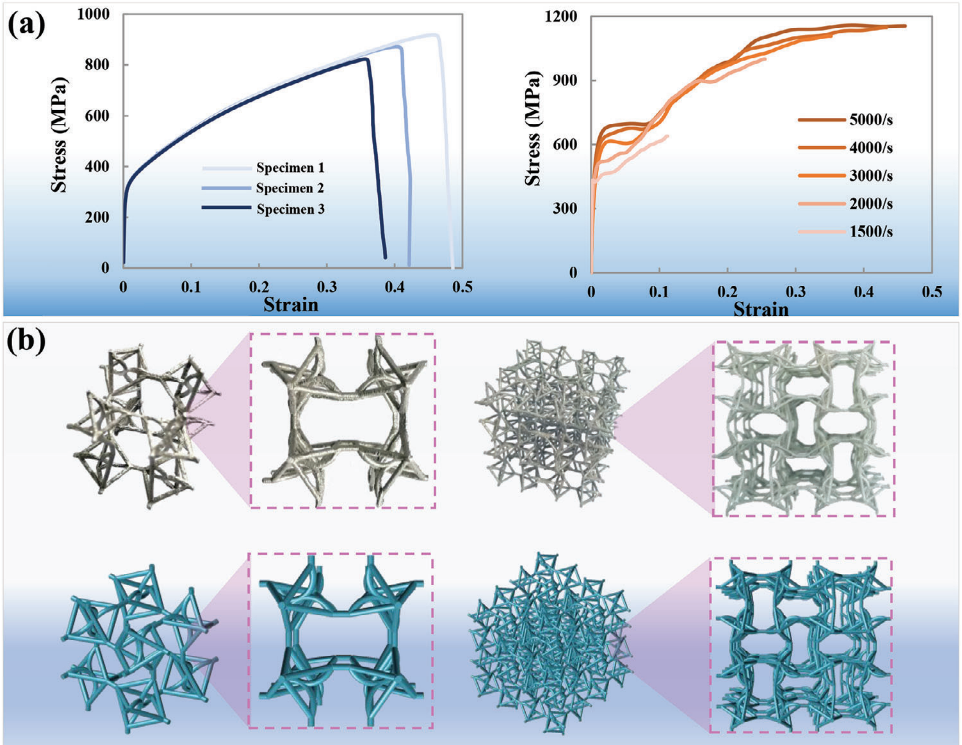

Figure 3. Manufacturing and testing. a) Quasi-static tensile and dynamic impact compression results for 316 L stainless steel. b) Processed specimens.

the relationships can be obtained according to Equations (4), (5), and (6).[42]

$$\sigma = \frac{A_0 E_0}{A}\,\varepsilon_t\,(t) \tag{4}$$

$$\dot{\varepsilon} = -\frac{2\sqrt{\frac{E_0}{\rho_0}}}{H}\varepsilon_r\,(t) \tag{5}$$

$$\varepsilon\,(t) = -\frac{2\sqrt{\frac{E_0}{\rho_0}}}{H}\int_0^t \varepsilon_r \mathrm{d}t \tag{6}$$

where $\varepsilon_t(t)$ and $\varepsilon_r(t)$ are the transmitted wave and the reflected wave, respectively. A_0 and E_0 are the cross-sectional area and the Young's modulus of the bars, respectively. ρ_0 is the density of the bars, A indicates the cross-sectional area summed over all struts in the multistrut sample, and H indicates the initial length of the sample in the loading direction.

The stress-strain curve obtained from the dynamic compression experiment is shown in **Figure 3**a. As the strain rate increases, the load curve and yield strength of the 316 L stainless steel material increase. Furthermore, periodic cells and $2 \times 2 \times 2$ cells of MM-ML are prepared using additive manufacturing technology. It can be observed that the outer surfaces of all specimens are relatively smooth and have good forming quality, which can be used for subsequent testing and analysis, as shown in Figure 3b.

3. Results and Discussion

3.1. Compression Behavior

The quasi-static and dynamic loading test and simulation results are shown in **Figure 4**. During the crushing process, the lateral volume of the MM-ML is compressed and exhibits a significant negative Poisson's ratio effect, which is consistent with the negative Poisson's ratio material deformation mode. Compared to some existing energy-absorbing metamaterials with a single loading effect (Figure 4e),[43–45] MM-ML (Figure 4c,d) can exhibit two distinct plateau stress characteristics. In the first plateau stress stage, the octahedral structures in MM-ML mainly undergo rotational behavior, while the connecting rods undergo bending. In the second plateau stress stage, adjacent connecting rods undergo geometric interference and contact extrusion, and the octahedral structures no longer undergo significant rotation. However, octahedral structures and double semicircular rods undergo bending extrusion until they reach the densification stage of the material. Metamaterials with multiple platform stress stages can effectively reduce the initial peak force and can undergo changes in different platform stresses during the crushing process. In addition, the structural deformation characteristics and load curve trends of the experimental and simulation results are highly consistent, which verifies the effectiveness of the numerical model established in this study. The experimental curve of dynamic impact has slight fluctuations, which may be caused by the high frequency of data collection and the uncertainty of rapid collisions. To explore the influence of different topological configuration parameters on the mechanical properties of MM-ML, the next

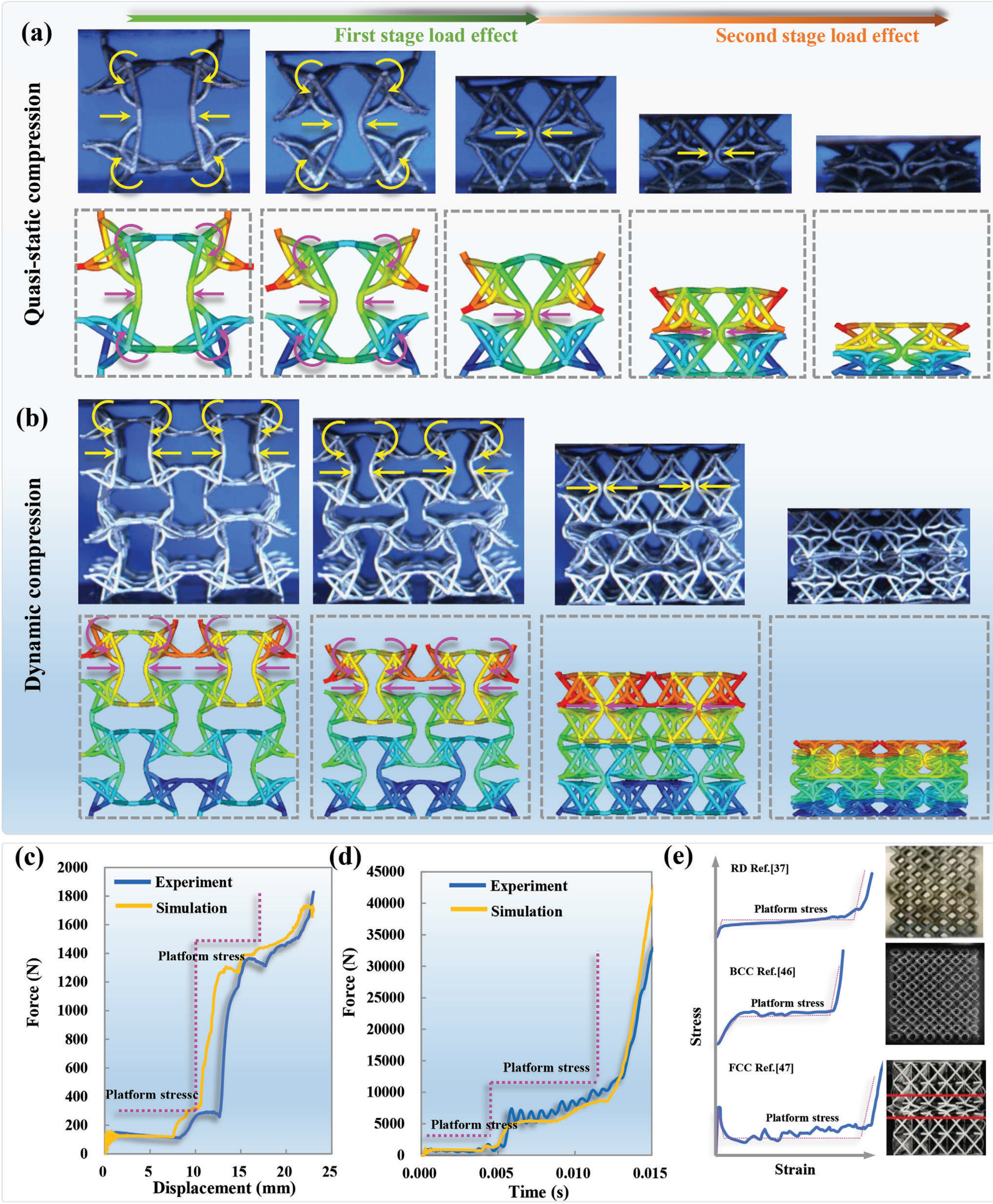

Figure 4. Numerical modeling and experimental results. a) Low-speed quasi-static compression deformation. b) Dynamic compression deformation. c) Low-speed quasi-static compression load curve. d) Dynamic compression load curves. e) Crushing forces of RD,[37] BCC,[46] and FCC.[47]

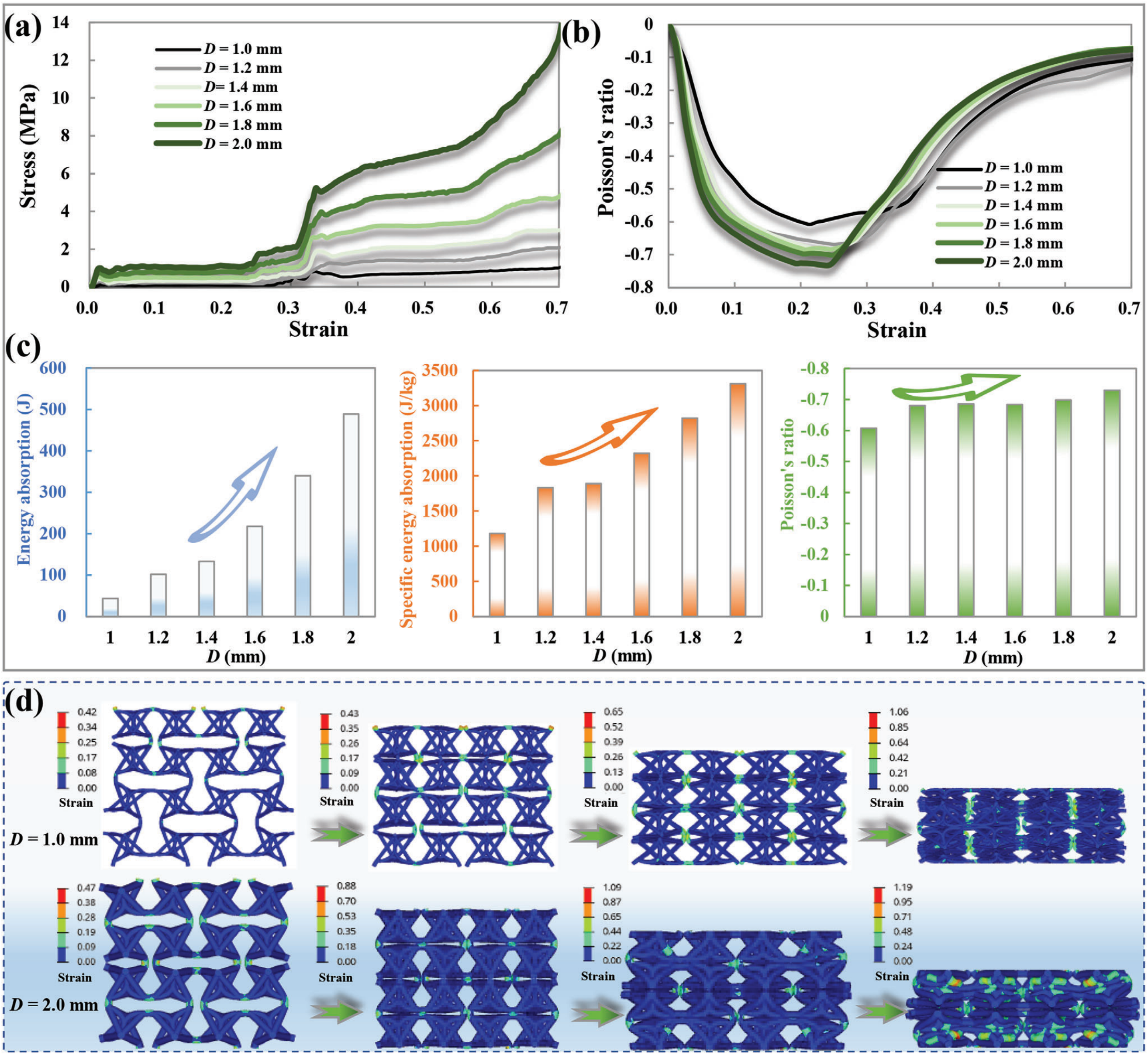

Figure 5. Analysis results for different rod diameters. a) Stress curves. b) Poisson's ratio curves. c) The energy absorption, specific energy absorption, and Poisson's ratio vary with this design parameter. d) Deformation characteristics of different compression processes (rod diameters of 1.0 and 2.0 mm).

section will analyze the influence of the rod diameter, rod size ratio, Euler angle, and cell arrangement using the validated numerical model.

3.2. Mechanical Properties

As shown in **Figure 5**a, the design space of different rod diameters for MM-ML from 1 mm to 2 mm is analyzed (a constant loading speed of 10 m^{-1} s, the same applies below), where the rotation angle is 20° and the lengths of the support rod and connecting rod are 9.6 and 3.39 mm, respectively. The configuration design of MM-ML is shown in Figure 2a. The stress curve began to significantly exhibit a second plateau stress when the compressive strain is ≈0.3. As the rod diameter increased, the stress gradually increased. At the same time, the increase in rod diameter resulted in an increase in the relative density of the MM-ML, and the compact strain gradually decreased. The generation of two plateau stresses in MM-ML stems from its special deformation behavior, where the octahedral structures undergo significant rotation during collapse, resulting in significant macroscopic volume shrinkage during compression. Therefore, this study also investigated the variation trend of Poisson's ratio, as shown in Figure 5b. As shown in Figure 2d, the calculation method for determining Poisson's ratio ν is as follows:

$$\nu = -\frac{\varepsilon_x}{\varepsilon_y} = -\frac{H}{W}\frac{\sum_{i=1}^{n}\left(\left|\Delta x_{A_i}\right| + \left|\Delta x_{B_i}\right|\right)}{n\Delta y} \tag{7}$$

where ε_x is the horizontal strain and ε_y is the longitudinal strain. H and W represent the height and width of MM-ML, respectively. Δx and Δy represent the horizontal and vertical displacements, respectively.

As the rod diameter increases, the range of Poisson's ratio gradually increases, with a maximum range of 0 to −0.73. Poisson's ratio gradually decreases within a strain range of 0 to 0.3, and when the strain is greater than 0.3, Poisson's ratio gradually increases until convergence. As the diameter of the rod increases, the range of the negative Poisson's ratio variation in the MM-ML during the crushing process tends to expand (Figure 5c). In addition, the energy absorption of MM-ML is also investigated. The energy absorption corresponding to the strain that did not enter the dense area (with a strain of 0.6) is adopted. As the rod diameter increases, the energy absorption capacity gradually increases, and when the diameter is 2 mm, the energy absorption can reach 489 J, and the specific energy absorption per unit mass can reach 3310 J/kg. When the diameter of the rod increases from 1 to 2 mm, the specific energy absorption per unit mass increases by 181%. The energy absorption capacity of MM-ML can increase with increasing material configuration.

To further reveal the main influence mechanism of different rod diameters on the mechanical properties of MM-MLs, the deformation behavior of MM-MLs with different rod diameters is analyzed. Figure 5d shows the deformation behavior of the MM-MLs with diameters of 1 and 2 mm. The maximum strain of the MM-ML occurs on the connecting rod during the initial compression stage, which is at a low-stress level, so the initial peak force is also at a low level. During the crushing process, an excessive initial peak load can cause damage to the protected object, so a crashworthy structure with superior protective capability should have a low initial stress level. As the nearby connecting rods are squeezed and the octahedral structures do not undergo significant rotation, strain gradually appears on all the rods. In this stage, all the octahedral structures are gradually compressed, and high platform stress levels appear until the structure is compacted.

The influence of the proportional relationship between the connecting rod and the supporting rod on the mechanical properties of MM-ML is analyzed here. The configuration design of MM-ML is shown in Figure 2b. The design space with different rod size ratios of 0.3 to 0.8 is analyzed, in which the rotation angle is 20° and the length of the supporting rod is 9.6 mm. Similarly, the stress curve begins to show the second platform stress significantly when the compressive strain is ≈0.3, and the stress level gradually decreases with increasing size ratio, as shown in **Figure 6a**. In contrast, with increasing size ratio, the variation range of Poisson's ratio gradually increases, and the maximum variation range is between 0–−0.67, as shown in Figure 6b,c.

The effect of energy absorption is also studied, as shown in Figure 6c. When the rod size ratio increases from 0.3 to 0.8, the specific energy absorption per unit mass decreases by 27%. With increasing rod size ratio, the energy absorption capacity gradually decreases, which may be mainly attributed to the fact that the larger the connecting rod size is, the more likely it is to lose stability under compression. The bearing capacity of MM-ML in the initial stage of compression decreases, and the mechanical properties of the octahedral structures are weakened. To further reveal the main mechanism of the influence of different rod size ratios on the mechanical properties of MM-ML, Figure 6d shows the deformation characteristics when the size ratio is 0.3 and 0.8. Under the same compression displacement, MM-ML with a low rod size ratio is more prone to material concentration, so it has a higher stress level, but MM-ML with a high rod size ratio is more prone to deformation, and its Poisson's ratio variation range is wider. In the feasible design space, a lower rod size ratio can increase the stress and energy absorption levels but also reduce the variation range of the Poisson's ratio. For some metamaterials with functional requirements, it is necessary to comprehensively consider the levels of various design parameters.

The Euler angle directly determines the attitude of the octahedral structures. Therefore, the influence of the Euler angle on the mechanical properties of MM-ML is also analyzed here, and the configuration design is shown in Figure 2c. The design space of MM-ML with different Euler angles ranged from 10–30°, where the diameter of the rod is 1.2 mm, and the lengths of the support rod and connecting rod are 9.6 and 3.39 mm, respectively. Interestingly, as the Euler angle increases, the platform stress range in the first stage gradually decreases. The first platform stress curve starts to step to the second platform stress at a strain of 0.15 when the Euler angle is 30°, as shown in **Figure 7a**. Compared with other Euler angles, the range of the first platform stress is significantly shorter. As the Euler angle increases, the variation range of Poisson's ratio tends to decrease, and the maximum range of variation is between 0 and −0.66, as shown in Figure 7b,c. When the Euler angle increases from 10° to 30°, the specific energy absorption per unit mass increases by 90%. As the Euler angle increases, the energy absorption capacity gradually increases, which may be mainly attributed to the fact that increasing the Euler angle provides more opportunities for the deformation of octahedral structures.

To further reveal the influence of different Euler angles on the mechanical properties of MM-ML, the deformation behavior of MM with different Euler angles is analyzed. Figure 7d shows the deformation characteristics with Euler angles of 10 – 30°. MM-ML with higher Euler angles is more prone to material concentration and has higher stress levels under the same compression displacement. However, MM-ML with higher Euler angles is more likely to step into the second platform stress. If it is necessary to balance different platform stress ranges, adjusting the Euler angle is a significant method. Customizing platform stress configurations at different stages through the strategy of controlling Euler angles can adapt to different collision protection needs.

As shown in **Figure 8a**, to further analyze the relationship between the above three design parameters (rod diameter, rod size ratio, and Euler angle) and the energy absorption performance, a 3D response surface for any two parameters is created by controlling the variables. The influence of three main design

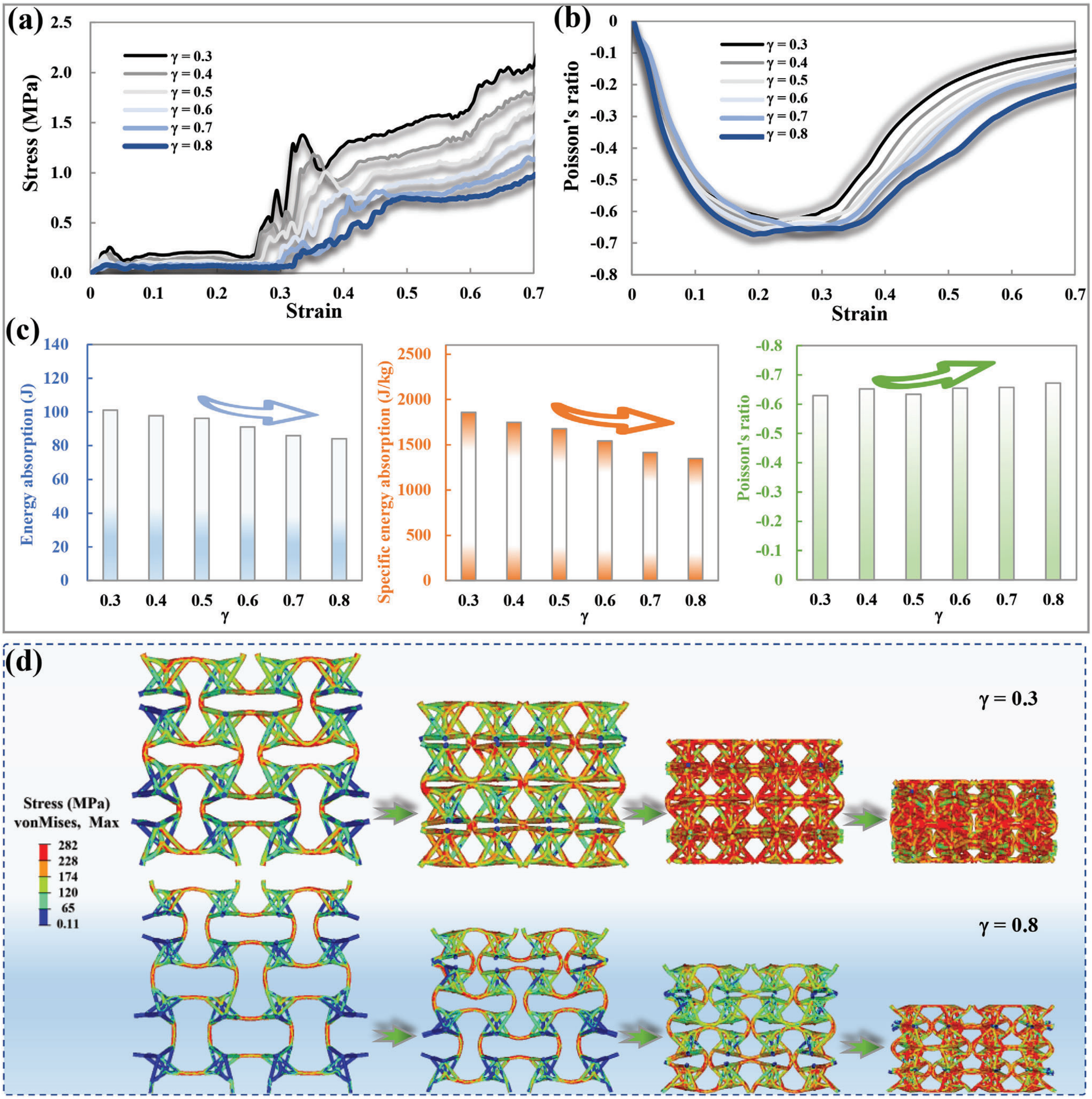

Figure 6. Analysis results for different rod size ratios. a) Stress curves. b) Poisson's ratio curves. c) The energy absorption, specific energy absorption, and Poisson's ratio vary with this design parameter. d) Deformation characteristics of different compression processes.

parameters on specific energy absorption exhibits a nonlinear mapping relationship. When keeping any design parameter constant, the other two design parameters are more likely to yield the maximum specific energy absorption at the boundary position of the design space. The research results can provide a reference for designers to develop excellent solutions.

The scale effect is a key topological parameter that needs to be considered because it can capture the evolution of the mechanical properties of MM-ML after expansion in different dimensions. By maintaining the same macroscopic region and weight, 2 × 2 × 2, 3 × 3 × 3, and 4 × 4 × 4 cell layouts are analyzed, and the configuration design is shown in Figure 2d. The rod diameter is 1.2 mm, the Euler angle is 20°, and the lengths of the support rod and connecting rod are 9.6 and 3.39 mm, respectively. Interestingly, as the number of cells increases, the first and second platform stress levels increase significantly, but the strains at which the second platform stress step occurs are similar (Figure 8b). Correspondingly, the energy absorption of MM-ML also significantly increases with increasing number of cells (Figure 8c,d). Under the premise of maintaining the same material weight and

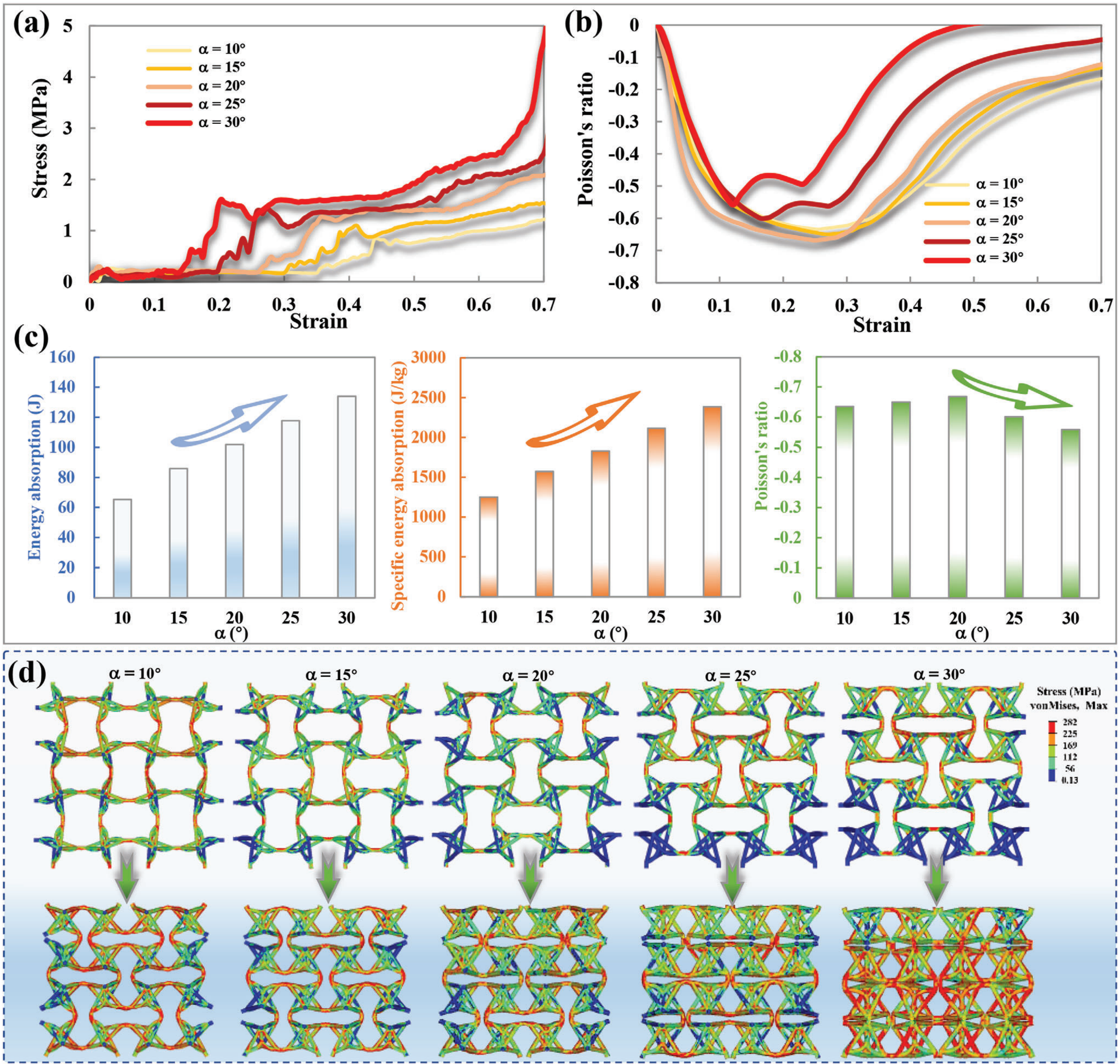

Figure 7. Analysis results for different Euler rotation angles. a) Stress curves. b) Poisson's ratio curves; c) Energy absorption, specific energy absorption, and Poisson's ratio vary with this design parameter. d) Deformation characteristics.

macroscopic volume, by doubling the topological number of cells, the specific energy absorption per unit mass can be increased by 51%. The deformation behavior of MM-MLs with different numbers of cells is analyzed in Figure 8e. The deformation characteristics with different compression displacements show that as the number of cells increases, the MM-ML can exhibit a uniform material distribution during the compression process, which is beneficial for improving the ability of the material to resist external deformation. Adjusting the number of MM-ML cells is an effective route for improving their mechanical properties without increasing the material weight.

4. Discussion

Compared with existing typical face-centered cubic metamaterials, body-centered cubic metamaterials, octahedral metamaterials, and honeycombs, the proposed MM-ML can exhibit a higher energy absorption potential at lower relative densities (**Figure 9a**). Moreover, according to recent data from other metamaterials, the specific strength and energy absorption exhibit a linear relationship in the logarithm plot (Figure 9b). The MM-ML performed reasonably close to the theoretical limit, which can lead to lightweight architected materials with high energy absorbance and high strength. Its mass-adjusted properties are superior to

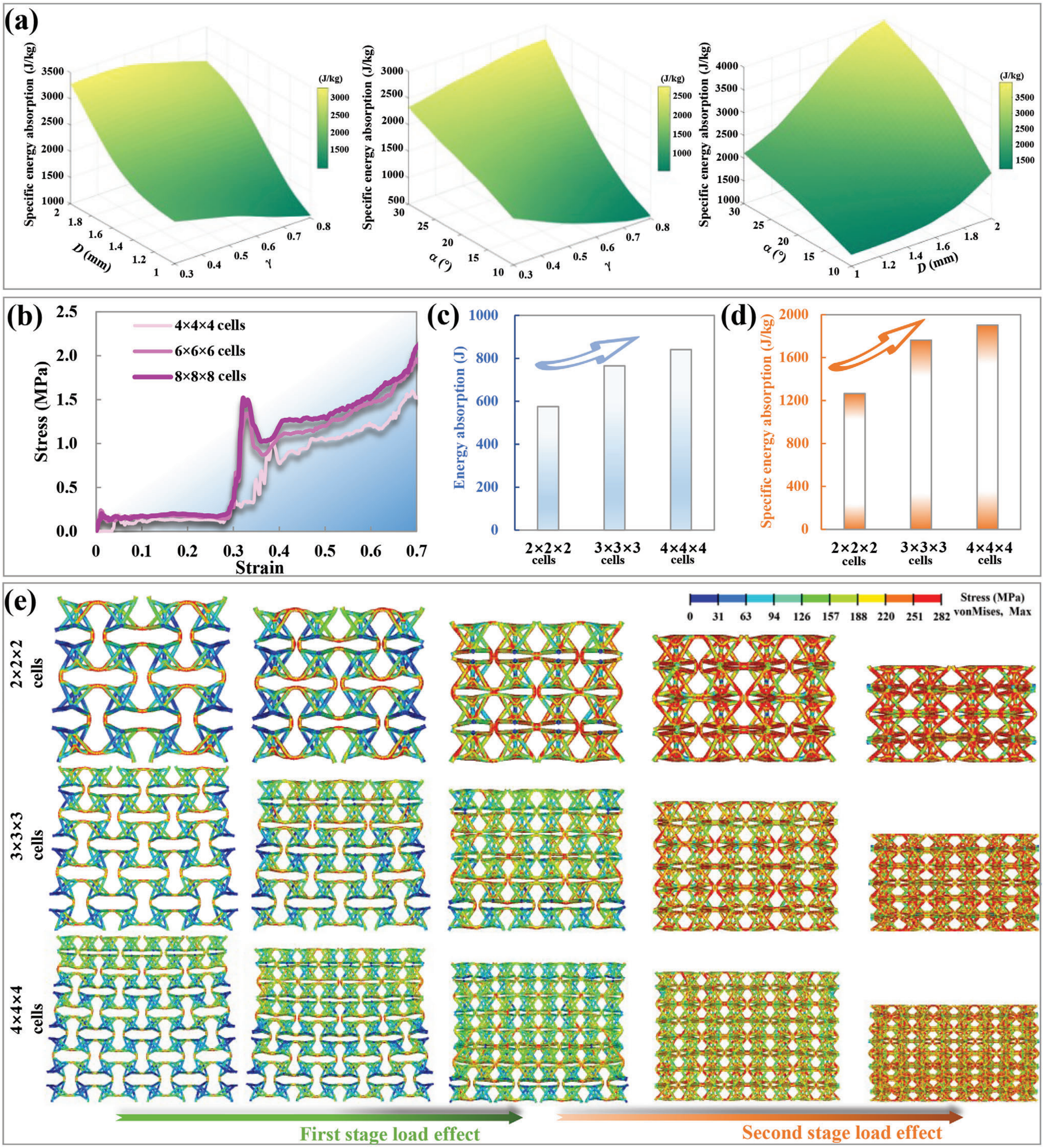

Figure 8. Analysis results of parameter effects and cell numbers. a) Parameter effects. b) Stress curves. c) Energy absorption curves. d) Specific energy absorption. e) Deformation characteristics.

those of other metamaterials. Compared with existing negative Poisson's ratio metamaterials, MM-ML also exhibits significant advantages, with a wide negative Poisson's ratio control region (Figure 9c). The design scheme proposed in this study has multiple advantages in terms of energy absorption, load-bearing capacity, and negative Poisson's ratio performance for lightweight materials, providing a solution for future lightweight innovative equipment protection design.

The energy absorption capacity of MM-ML, an energy-absorbing material for collision protection, should be further

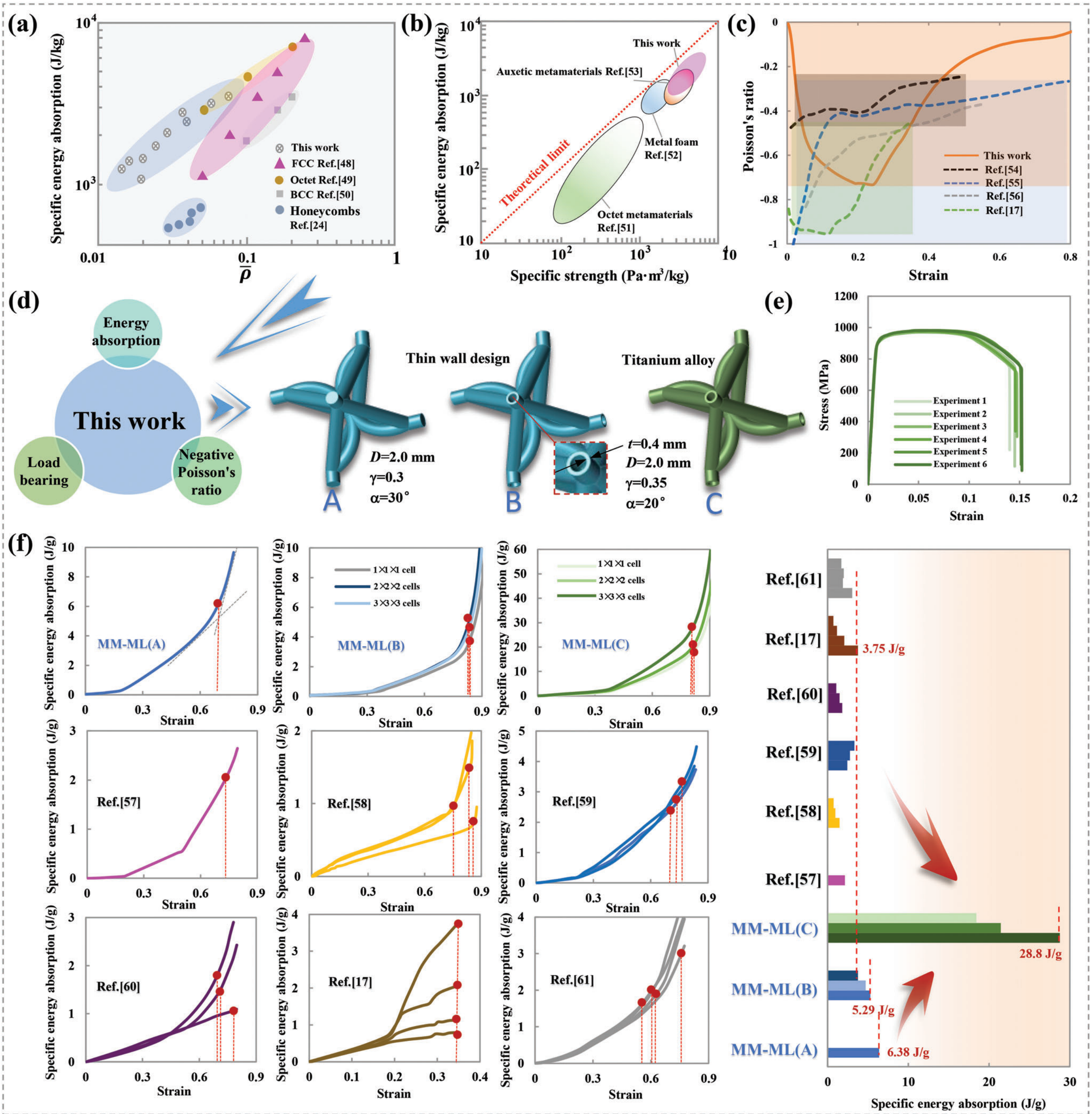

Figure 9. Advantages of MM-MLs. a) Comparison of energy absorption under different relative densities: FCC,[48] Octet,[49] BCC,[50] and honeycombs.[24] b) Comparison of energy absorption under different specific strengths: octet metamaterials,[51] metal foams,[52] and auxetic metamaterials.[53] c) Negative Poisson's ratio range of different metamaterials,[54,55,17,56] d) Improved methods for achieving higher energy absorption. e) Tensile mechanical curves of titanium alloys. f) Specific energy absorption of metamaterials of the same type.[17,57–61]

evaluated. Based on the above analysis, three design schemes that can be used to improve the energy absorption potential are provided, as shown in Figure 9d. Scheme A: Select the boundary values of the design parameters; Scheme B: Adopt a hollow thin-walled design; Scheme C: Use a lighter and stronger material (titanium alloy). The six sets of repeated tensile test data for the titanium alloy materials are presented in Figure 9e. As shown in Figure 9f, the maximum energy absorption of metamaterials should be evaluated by selecting values close to the dense region. For example, the specific energy absorption of MM-ML (A) can be obtained by calculating the curve inflection point. Compared with metamaterials with multi-level loading effects and negative Poisson's ratio characteristics in existing research, the three schemes achieved higher specific energy absorption than did the metamaterials introduced in the literature. The specific energy absorption of MM-ML (A) can be increased by 70% compared to that of the same type of metamaterial, the specific energy absorption of MM-ML (B) can be increased by 41% compared to that of the same type of metamaterial, and the specific energy absorption of MM-ML (C) can be increased by 667% compared to that of the same type of metamaterial without changing the design principle. This further demonstrates the potential advantages of the metamaterial design method proposed in this study in the field of energy absorption.

5. Conclusion

Based on octahedral structures, this study designed a mechanical metamaterial with multi-level loading effects through coordinate transformation and a mirror array. MM-ML exhibits significant two-level platform stress, and during the first stage of platform stress, local cells of MM-ML undergo rotational motion. During the second stage of platform stress, MM-ML mainly exhibits collapse compression and bending. Due to the differential deformation exhibited by MM-ML during different compression stages, Poisson's ratio of MM-ML is negative within the strain interval exhibited during the first stage of platform stress and gradually decreases. The diameter and length ratio of the support rod and connecting rod in MM-ML have a significant impact on the platform stress level. Within the predetermined design space, a higher rod diameter can produce higher load levels and can increase the range of negative Poisson's ratio regulation, increasing the potential for energy absorption. Although appropriately increasing the length of the connecting rod can increase the range of Poisson's ratio, it will reduce the platform stress level and energy absorption. By adjusting the Euler angles, the strain ranges of the first and second platform stresses can be effectively regulated. Increasing the Euler angles reduces the strain range of the first platform stress and improves the energy absorption capacity. Additionally, increasing the number of cells while maintaining a constant relative density can effectively enhance energy absorption without significantly changing the strain ranges of the first and second platform stresses. MM-ML with multi-level load effects has significant parameter controllability and can adjust its topology according to the needs of the application scenarios to achieve different platform stress regions, different ranges of Poisson's ratios, and different energy absorption requirements. As an energy-absorbing material for impact protection, it has a higher specific energy absorption than existing metamaterials of the same type, which provides a feasible solution for the protection design of future lightweight equipment.

6. Experimental Section

Specimen Fabrication: A laser powder bed fusion (LPBF) LIM-X260A machine (Tianjin LiM Laser Technology Co., Ltd., China) is used for all material fabrication. 316 L stainless steel is utilized as the printing material. The printer parameters included a laser power of 285 W, a laser beam diameter of 0.085 mm, a layer thickness of 40 µm, and a scanning speed of 950 mm $^{-1}$s.

Quasi-Static Test: The basic mechanics of the stainless steel materials are evaluated using a universal testing machine at a speed of 1 mm/min. The stress σ versus strain ε curves are plotted after compression, and the following classical mechanical evaluation indicators are calculated from these curves, as shown in Figure S1a (Supporting Information). The low-speed quasi-static compression test of the metamaterials is carried out by a universal material testing machine at a speed of 2 mm/min. The key deformation processes are captured by a camera, as shown in Figure S1c (Supporting Information).

Dynamic Test: A split Hopkinson pressure bar (SHPB) is used to evaluate the strain rates of the stainless steel materials, which are 1500, 2000, 3000, 4000, and 5000 s^{-1}. The signals are evaluated in the form of the engineering stress σ, strain rate $\dot{\varepsilon}$, and strain ε, and the relationships can be obtained according to Equations (4), (5), and (6). The dynamic mechanical tests of the metal materials are presented in Figure S1b (Supporting Information). The dynamic compression test of the MM-ML is performed on a drop hammer testing machine (Shenzhen Tianyi Technology Co., Ltd.). A high-speed camera is used to capture the deformation patterns of short-term impacts. The height of the hammer is 1000 mm, the size of the hammerhead is 100 × 100 mm, and the hammer weight is 30.62 kg, as shown in Figure S1d (Supporting Information).

Simulation: Finite element analysis (FEA) is adopted for the analysis of the deformation mechanisms. LS-DYNA software is used to carry out the numerical simulations. The general explicit algorithm is suitable for solving highly nonlinear problems involving contact and large deformations. All the metamaterials are modeled using a piecewise linear elastic-plastic strain hardening material. The material properties include an elastic modulus of 190.57 GPa, a yield strength of 282.77 MPa, a density of 7.98 g cm^{-3}, and a Poisson's ratio of 0.3. The Cowper-Symonds constitutive model was used to define the mechanical behavior of 316 L stainless steel, and its constitutive relationship is expressed as follows[62–63]:

$$\sigma_y = \sigma_y^s \left[1 + \left(\frac{\dot{\varepsilon}}{C} \right)^{\frac{1}{P}} \right] \tag{7}$$

where σ_y represents the yield stress at the current strain rate, σ_y^s represents the yield stress under quasi-static compression, and $\dot{\varepsilon}$ represents the current strain rate. C and P are constants obtained by performing curve fitting with the experimental data. Based on the different strain rate load data obtained in Fig. 3(b), $C = 335$ and $P = 0.26$ are ultimately obtained.

Supporting Information

Supporting Information is available from the Wiley Online Library or from the author.

Acknowledgements

This work was financially supported by the Anhui Provincial Natural Science Foundation (2308085QE158), the National Natural Science Foundation of China (No. 52305244 and U22B2013), and the Beijing Nova Program (20230484287).

Conflict of Interest

The authors declare no conflict of interest.

Data Availability Statement

The data that support the findings of this study are available from the corresponding author upon reasonable request.

Keywords

Dynamic impact, energy absorption, metamaterials, multi-level crushing effects

Received: April 17, 2024
Revised: June 13, 2024
Published online:

[1] T. T. Li, Y. N. Li, *Adv. Mater.* **2024**, *36*, 2309604.
[2] S. J. Park, J. H. Lee, J. Yang, W. Heogh, D. Kang, S. M. Yeon, S. H. Kim, S. Hong, Y. Son, J. Park, *J. Manuf. Processes* **2022**, *79*, 759.
[3] L. Peng, B. Bao, *Eng. Struct.* **2023**, *292*, 116550.
[4] H. F. Yin, W. Z. Zhang, L. C. Zhu, F. B. Meng, J. E. Liu, G. L. Wen, *Composite. Struct.* **2023**, *304*, 116397.
[5] H. R. Zhang, H. Zhou, Z. X. Zhou, H. Z. Zeng, X. Y. Zhang, J. Z. Yang, H. S. Lei, F. S. Han, *Int. J. Solids Struct.* **2021**, *226*.
[6] H. Jiang, B. A. Bednarcyk, L. L. Barbenchon, Y. Chen, *Thin-Walled Struct.* **2023**, *192*, 111115.
[7] X. Q. Lan, S. Q. Yang, Y. Dong, Z. M. Wang, H. Li, *Int. J. Mech. Sci.* **2024**, *263*, 108791.
[8] J. Noronha, J. Dash, J. Rogers, M. Leary, M. Brandt, M. Qian, *Adv. Mater.* **2024**, 2308715, https://doi.org/10.1002/adma.202308715.
[9] H. Zhong, R. Das, J. Gu, M. Qian, *Mater. Today* **2023**, *68*, 96.
[10] B. V. S. Reddy, A. M. Shaik, D. Sundeep, C. S. Chebiyyam, J. Krishnaiah, U. Chandrasekhar, *Transact. of the Indian Institute of Metals* **2024**, *77*, 615.
[11] B. J. R. Smeets, E. M. Fagan, K. Matthews, R. Telford, B. R. Murray, L. Pavlov, B. Weafer, P. Meier, J. Goggins, *Composites Part B-ENG.* **2021**, *212*, 108691.
[12] H. Jiang, H. Ziegler, Z. N. Zhang, H. Zhang, L. L. Barbenchon, S. Atre, Y. Y. Chen, *Composites Part B-Eng.* **2022**, *236*, 109809.
[13] L. R. Meza, A. J. Zelhofer, N. Clarke, A. J. Mateos, D. M. Kochmann, J. R. Greer, *Proc. Nat. Acad. Sci.* **2015**, *112*, 11502.
[14] Q. Wang, J. A. Jackson, Q. Ge, J. B. Hopkins, C. M. Spadaccini, N. X. Fang, *Phys. Rev. Lett.* **2016**, *117*, 175901.
[15] X. Wu, S. Wang, Y. Ma, Z. Deng, *Mech. Adv. Mater. Struct.* **2024**, *31*, 1348.
[16] Z. Gao, H. Wang, H. Sun, T. Sun, Y. Wu, C. L. A. Leung, H. Wang, *Composites Part B: Eng.* **2022**, *247*, 110345.
[17] D. Han, X. Ren, C. Luo, Y. Zhang, X. Y. Zhang, X. G. Zhang, W. Jiang, J. Hao, Y. M. Xie, *Addit. Manuf.* **2022**, *55*, 102789.
[18] S. Zhou, H. Liu, J. Ma, X. Yang, J. Yang, *Aero. Sci. Technol.* **2023**, *142*, 108583.
[19] C. S. Ha, M. E. Plesha, R. S. Lakes, *Smart Mater. Struct.* **2016**, *25*, 054005.
[20] F. Li, Q. Zhang, Z. Wang, D. Zhu, *Eng. Struct.* **2024**, *306*, 117793.
[21] X. G. Zhang, W. Jiang, Y. Zhang, D. Han, C. Luo, X. Y. Zhang, J. Hao, Y. M. Xie, X. Ren, *Thin-Walled Struct.* **2023**, *188*, 110829.
[22] L. Li, F. Yang, S. Zhang, Z. Guo, L. Wang, X. Ren, M. Zhao, *Eng. Struct.* **2023**, *289*, 116335.
[23] L. Mizzi, A. Spaggiari, *Smart Mater. Struct.* **2020**, *29*, 105036.
[24] S. Qin, X. Deng, F. Yang, Q. Lu, *Compos. Struct.* **2023**, *323*, 117493.
[25] E. T. Zhang, H. Liu, B. F. Ng, *Composites, Part B* **2021**, *227*, 109366.
[26] H. Lu, X. Wang, T. Chen, *Thin-Walled Struct.* **2022**, *179*, 109757.
[27] V. Sinđelić, A. Nikolić, G. Minak, N. Bogojević, S. Ć. Kostić, *Mater. Today Commun.* **2023**, *37*, 107593.
[28] A. Montazeri, A. Saeedi, E. Bahmanpour, M. Mahnama, *Int. J. Mech. Sci.* **2024**, *266*, 108917.
[29] C. Mercer, T. Speck, J. Lee, D. S. Balint, M. Thielen, *Int. J. Impact Eng.* **2022**, *169*, 104315.
[30] Y. Zhao, Y. Wang, J. Hao, Y. Wang, K. Wang, S. Tai, *Compos. Struct.* **2023**, *322*, 117348.
[31] J. Cui, L. Zhang, A. K. Gain, *Int. J. Mech. Sci.* **2023**, *260*, 108614.
[32] Z. Li, W. Gao, M. Y. Wang, C. H. Wang, Z. Luo, *Int. J. Mech. Sci.* **2023**, *259*, 108617.
[33] J. Wang, X. Luo, K. Wang, S. Yao, Y. Peng, *Compos. Struct.* **2022**, *298*, 115999.
[34] T. Wang, J. An, H. He, X. Wen, X. Xi, *Compos. Struct.* **2021**, *262*, 113663.
[35] J. Ye, Z. Sun, Y. Ding, Y. Zheng, F. Zhou, *Thin-Walled Struct.* **2023**, *190*, 110988.
[36] Q. Zhang, B. Li, S. Zhou, M. Luo, F. Han, C. Chai, J. Wang, X. Yang, *Int. J. Mech. Sci.* **2024**, *264*, 108834.
[37] L. Xiao, X. Xu, G. Feng, S. Li, W. Song, Z. Jiang, *Int. J. Mech. Sci.* **2022**, *219*, 107093.
[38] L. Xiao, G. Shi, G. Feng, S. Li, S. Liu, W. Song, *Int. J. Solids Struct.* **2024**, *296*, 112830.
[39] F. S. H. B. Freeman, L. M. Jones, A. D. Goodall, H. Ghadbeigi, I. Todd, *Additive Manufact. Lett.* **2024**, *8*, 100190.
[40] D. Zheng, R. Li, J. Kang, M. Luo, T. Yuan, C. Han, *Int. J. Machine Tools and Manufact.* **2024**, *195*, 104110.
[41] X. Wang, R. Qin, J. Lu, M. Huang, X. Zhang, B. Chen, *Mater. Des.* **2024**, *238*, 112659.
[42] R. Gümrük, R. A. W. Mines, S. Karadeniz, *J. Mater. Eng. Perform.* **2018**, *27*, 1016.
[43] X. Wang, X. Li, Z. Li, Z. Wang, W. Zhai, *Small* **2024**, *20*, 2307369.
[44] J. Tang, H. Liang, A. Ren, L. Ma, W. Hao, Y. Yao, L. Zheng, H. Li, Q. Li, *Adv. Mater.* **2024**, *36*, 2400080.
[45] R. Hamzehei, A. Serjouei, N. Wu, A. Zolfagharian, M. Bodaghi, *Adv. Eng. Mater.* **2022**, *24*, 2200656.
[46] L. Bai, C. Gong, X. Chen, J. Zheng, J. Yang, K. Li, Y. Sun, *Int. J. Mech. Sci.* **2022**, *214*, 106922.
[47] C. Li, J. Qi, P. Wang, Z. Zhao, Z. Wang, H. Lei, S. Duan, *Sci. China Phys., Mech. Astron.* **2022**, *65*, 294611.
[48] N. Jin, F. Wang, Y. Wang, B. Zhang, H. Cheng, H. Zhang, *Mater. Des.* **2019**, *169*, 107655.
[49] T. Tancogne-Dejean, A. B. Spierings, D. Mohr, *Acta Mater.* **2016**, *116*, 14.
[50] S. Yuan, C. K. Chua, K. Zhou, *Adv. Mater. Technol.* **2019**, *4*, 1800419.
[51] M. Mohsenizadeh, F. Gasbarri, M. Munther, A. Beheshti, K. Davami, *Mater. Des.* **2018**, *139*, 521.
[52] P. Schüler, S. F. Fischer, A. Bührig-Polaczek, C. Fleck, *Mater. Sci. Eng., A* **2013**, *587*, 250.
[53] Q. Wang, Z. Yang, Z. Lu, X. Li, *Mater. Des.* **2020**, *186*, 108226.
[54] W. Z. Jiang, X. C. Teng, X. H. Ni, X. G. Zhang, X. Cheng, W. Jiang, D. Han, Y. Zhang, X. Ren, *Eng. Struct.* **2024**, *301*, 117318.
[55] N. Ma, S. Han, Q. Han, C. Li, *Thin-Walled Struct.* **2024**, *198*, 111652.
[56] X. C. Teng, X. Ren, Y. Zhang, W. Jiang, Y. Pan, X. G. Zhang, X. Y. Zhang, Y. M. Xie, *Int. J. Mech. Sci.* **2022**, *229*, 107524.
[57] H. Lu, X. Wang, T. Chen, *Compos. Struct.* **2022**, *291*, 115591.
[58] M.-R. An, L. Wang, H.-T. Liu, F.-G. Ren, *Thin-Walled Struct.* **2022**, *170*, 108530.
[59] N. Li, S.-z. Liu, X.-n. Wu, J.-y. Wang, Y.-s. Han, X.-c. Zhang, *Thin-Walled Struct.* **2023**, *191*, 111081.
[60] C. Qi, F. Jiang, A. Remennikov, L.-Z. Pei, J. Liu, J.-S. Wang, X.-W. Liao, S. Yang, *Composites, Part B* **2020**, *197*, 108117.
[61] X. Zhang, X. Wu, W. Wu, L. Wang, *Soil Dynamics, and Earthquake Eng.* **2023**, *171*, 107972.
[62] O. Červinek, H. Pettermann, M. Todt, D. Koutný, O. Vaverka, *J. Mater. Res. Technol.* **2022**, *18*, 3684.
[63] R. Gümrük, R. A. W. Mines, *Int. J. Mech. Sci.* **2013**, *68*, 125.

